ARTICLE

Fused-Ring Pyrazine Derivatives for n-Type Field-Effect Transistors

Haifeng Wang,† Yugeng Wen,† Xiaodi Yang, Ying Wang, Weiyi Zhou,† Shiming Zhang,† Xiaowei Zhan,* Yunqi Liu,* Zhigang Shuai, and Daoben Zhu*

Beijing National Laboratory for Molecular Sciences and CAS Key Laboratory of Organic Solids, Institute of Chemistry, Chinese Academy of Sciences, Beijing 100190, China

ABSTRACT Three new fused-ring pyrazine derivatives end-functionalized with trifluoromethylphenyl groups have been synthesized. The effect of a fused-ring pyrazine core on the thermal, electronic, optical, thin film morphology, and organic field-effect transistor (OFET) properties was investigated both experimentally and theoretically. Electrochemistry measurements and density functional theory calculations suggest that the pyrazine core plays a significant role in tuning the electron affinities of these compounds. The optical absorption and fluorescence properties are also sensitive to the pyrazine core. The OFET devices based on the fused-ring pyrazine compounds exhibit electron mobilities as high as ca. 0.03 $cm^2 V^{-1} s^{-1}$ under nitrogen, and their performance is sensitive to the pyrazine core. The larger pyrazine core leads to a lower LUMO level and lower reorganization energy, to more ordered thin film morphology with larger grain size, and finally to higher mobilities.

KEYWORDS: n-type organic semiconductor • field-effect transistor • fused-ring pyrazine • synthesis • density functional theory • structure−property relationship

INTRODUCTION

Organic field-effect transistors (OFETs) based on organic semiconductors have attracted great attention because of their potential applications in low-cost, lightweight, and flexible large-area plastic circuits, such as flat display, radio-frequency identification tags, electronic papers, and smart memory/sensor elements (1). Since the first report on OFETs in 1986 (2), there has been great progress in both organic semiconductors and device fabrication techniques. The performance of p-type OFETs is comparable to that of the amorphous silicon-based FETs (3). On the other hand, n-type organic semiconductors are important for the fabrication of organic p−n junctions, ambipolar transistors, and complementary circuits (1). However, excellent n-type organic semiconductors with high electron affinity (EA), high electron mobility, and good environmental stability still remain rare (1, 4). To achieve high-performance n-type OFETs, the organic semiconductors should have strong intermolecular interactions and a proper lowest unoccupied molecular orbital (LUMO) energy level near to the work function of the source/drain electrodes (4). In recent years, to lower the LUMO levels of organic semiconductors, electron-withdrawing groups, such as fluorine, cyano, or carbonyl groups, were introduced into pentacene and oligothiophene derivatives (5), which are known as hole-transporting systems. Although these compounds usually have proper LUMO energies for n-type OFETs, some of them do not have sufficient intermolecular interactions (5d, 6), which could limit intermolecular electron hopping and, therefore, decrease the performance of n-type OFETs.

Recently, Yamashita et al. reported that several N- and S-containing heterocyclic oligomers with trifluoromethylphenyl groups exhibited low LUMO levels, tightly packing structure, and good n-type OFET performance (7). The heterocyclic units, such as thiazole (7a, 7g), thiazolothiazole (7b, 7c), and benzothiadiazole (7d−7f), can improve the intermolecular interactions due to $\pi-\pi$ stacking as well as heteroatom contact. As another kind of heterocyclic derivative, N-containing oligoacenes have also been proven to be promising candidates for n-type semiconductors (8). The existence of electron-withdrawing imine nitrogen atoms (=N−) increases the EA. The CH−N hydrogen bonding and polar−polar interactions induce strong intermolecular interactions and facilitate the formation of a highly ordered and dense packing structure, which is helpful to the electron-transport and kinetic stability to oxygen and moisture (9). Moreover, replacing the CH moieties with nitrogen atoms can improve stability toward photooxidation or Diels−Alder dimerization (two major degradation pathways in pentacene semiconductors) (9). As one of the typical nitrogen-rich heterocycles, pyrazine is used as a building block in the design and synthesis of n-type organic semiconductors (10); some pyrazine derivatives exhibit high electron mobilities (11).

We have interest in fused-ring pyrazine derivatives end-functionalized with trifluoromethylphenyl groups based on the following considerations: (a) molecules containing fused-ring systems tend to maximize the π-orbital overlap by restricting intramolecular rotation in the oligomer and possibly to induce highly ordered π stacking (12); (b) trifluo-

* Corresponding authors. E-mail: xwzhan@iccas.ac.cn (X.Z.), liuyq@iccas.ac.cn (Y.L.), zhudb@iccas.ac.cn (D.Z.).
Received for review February 12, 2009 and accepted April 6, 2009
† Also at Graduate University of Chinese Academy of Sciences, Beijing 100039, China.
DOI: 10.1021/am900093p

Published on Web 04/29/2009

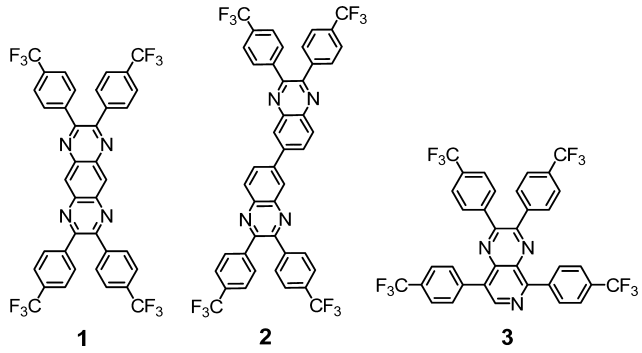

FIGURE 1. Chemical structures of 1−3.

Scheme 1. Synthesis of Compounds 1−3

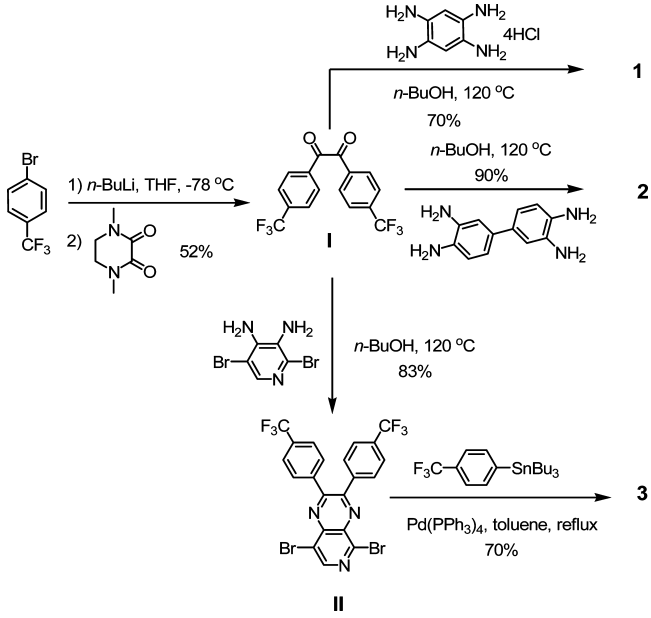

romethylphenyl groups could further increase the EA and are favorable for molecular alignment (7). Here, we report the synthesis, characterization, and OFET properties of three fused-ring pyrazine derivatives functionalized with four trifluoromethylphenyl groups (**1**−**3**, Figure 1). In addition, we investigated the impact of the core structure on the electronic and optical properties, thin film morphology, and OFET performance.

RESULTS AND DISCUSSION

Synthesis. The synthetic routes to **1**−**3** are described in Scheme 1. All compounds were easily synthesized in high yields from commercial starting materials. At first, the reaction between 1,4-dimethylpiperazine-2,3-dione and a lithium reagent, which was generated in situ from 1-bromo-4-(trifluoromethyl)benzene and a *n*-BuLi reagent at −78 °C, gave rise to 4,4′-bis(trifluoromethyl)benzil (**I**) in 52% yield. The benzil was treated with benzene-1,2,4,5-tetraamine tetrahydrochloride, biphenyl-3,4,3′,4′-tetraamine, and 2,5-dibromopyridine-3,4-diamine in *n*-butanol to give **1**, **2**, and **II** in 70%, 90%, and 83% yield, respectively. **3** was synthesized by Stille coupling between **II** and tributyl[4-(trifluoromethyl)phenyl]stannane in 70% yield. The three compounds are soluble in common organic solvents such as

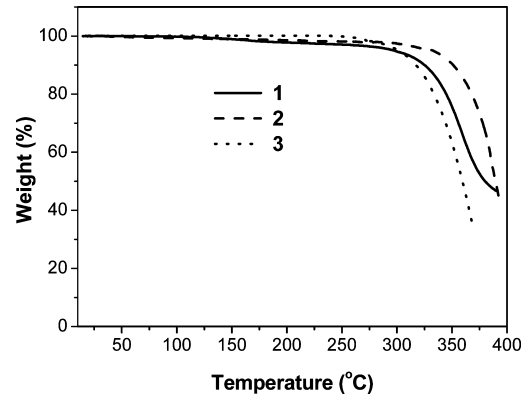

FIGURE 2. TGA curves of 1−3.

dichloromethane, tetrahydrofuran (THF), and chloroform, which allowed us to purify them conveniently through column chromatography and recrystallization. The thermal properties of the compounds were determined by thermogravimetric analysis (TGA). They possess good thermal stability with onset weight-loss temperatures of over 300 °C (Figure 2).

Photophysical Properties. The UV−vis absorption and photoluminescence (PL) properties of the compounds in solution and in the thin film have been investigated (Figure 3), and the spectral data are summarized in Table 1. The absorption and emission spectra are closely associated with the different core structures of the pyrazine derivatives. **1**−**3** exhibit two absorption bands at 276−309/405−419, 285/377, and 270/353 nm, respectively. Clearly, the absorption spectra in solution red shift upon expansion of the fused-ring core. Absorption in the solid state for **1**−**3** is similar to that in solution with only modest red shifts. The optical energy gaps of **1**−**3** are estimated from the absorption edge of the thin films; they are 2.73, 3.00, and 2.84 eV, respectively. It is well-known that, of all of the organic semiconductor materials reported so far, pentacene is currently a benchmark with the highest mobility (13). However, it suffers from oxidation instability with an energy gap of around 1.85 eV (14). The energy gaps of these materials are much larger than that of pentacene, suggesting that **1**−**3** are relatively stable toward photooxidation. Among these compounds, **1** has the smallest energy gap. It is generally recognized that increasing the planarity and conjugation of aromatic systems leads to a decrease in the energy gap.

1−**3** show blue luminescence at 460, 410, and 405 nm, respectively, paralleling the changes in the absorption spectra. The Stokes shifts for **1**−**3** in solution are 54, 33, and 51 nm, respectively. The relatively large Stokes shifts suggest that the molecules undergo considerable molecular rearrangement upon photoexcitation, leading to a big structural difference between the excited and ground states (15). Thin films of **2** and **3** emit fluorescence peaked at 440 and 486 nm, while no emission was observed for **1** in the solid state, probably because of aggregation-induced PL quenching (16), caused by the larger coplanar fused-ring core and stronger intermolecular interaction.

Electrochemistry. Figure 4 shows cyclic voltammograms of **1**−**3**. All compounds exhibit one (**3**) or two (**1** and

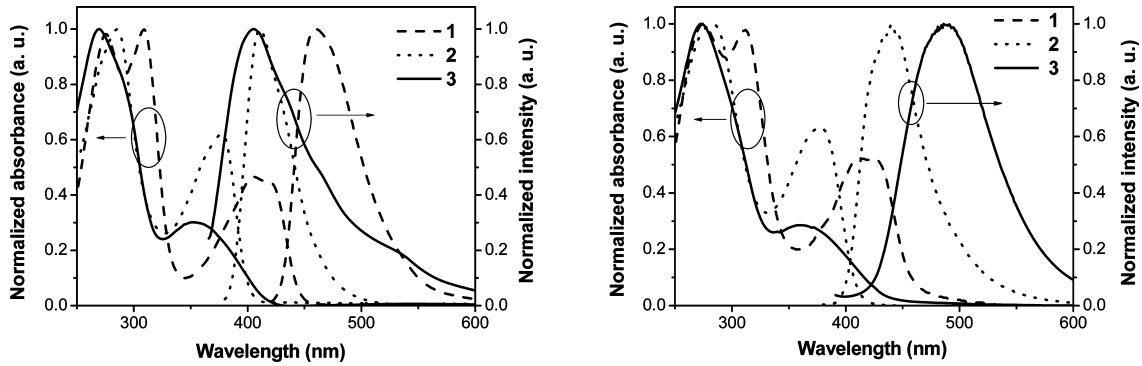

FIGURE 3. UV−vis and PL spectra of 1 (dashed line), 2 (dotted line), and 3 (solid line) in a dichloromethane solution (left) and in the solid state (right).

Table 1. Absorption and Emission Characteristics for 1−3

	absorption maxima (nm)		emission maxima (nm)	
compounds	solution[a]	film	solution[a]	film
1	309, 406	312, 412	460	
2	285, 378	284, 377	411	440
3	270, 354	273, 360	405	486

[a] In CH_2Cl_2.

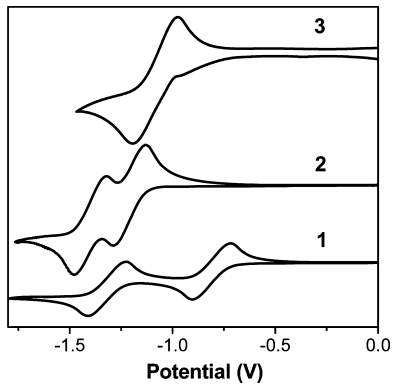

FIGURE 4. Cyclic voltammograms for 1−3 in CH_2Cl_2/0.1 M $[^nBu_4N]^+[PF_6]^-$ with ferrocenium/ferrocene as an internal standard, at 50 mV s^{-1}. The horizontal scale refers to an anodized Ag wire pseudoreference electrode.

2) perfectly reversible reduction waves, suggesting that they have excellent electrochemical stability. No oxidation peaks were observed, indicating that they are intrinsic n-type organic semiconductors. The LUMO energies were estimated from the reduction potentials $E_{1/2}$, assuming the absolute energy level of ferrocene/ferrocenium to be 4.8 eV below vacuum. The LUMO levels of **1**−**3** are −3.5, −3.0, and −3.2 eV, respectively (Table 2), which are suitable for n-type OFET. The lower LUMO of **1** is probably due to its larger core with higher pyrazine density.

The calculated highest occupied molecular orbital (HOMO) and LUMO wave functions of compounds **1**−**3** are depicted in Figure 5. The coefficients in the LUMO are mostly localized on the N-containing oligoacene, indicating the feasibility for intermolecular electron transfer (ET). Estimates of the HOMO and LUMO levels are shown in Table 2. The calculated HOMOs for the three compounds are similar, resembling the trend in HOMOs calculated from LUMOs and optical energy

Table 2. Experimental Estimates and DFT Calculations of HOMO and LUMO[a]

	HOMO		LUMO	
compounds	experimental[b]	B3LYP/ 6-31g(d)	experimental[c]	B3LYP/ 6-31g(d)
1	−6.29	−6.60	−3.50	−3.24
2	−6.11	−6.44	−3.02	−2.69
3	−6.20	−6.53	−3.22	−3.02

[a] All energies are in electronvolts. [b] Calculated from the LUMO and optical energy gap estimated from the absorption edge in solution. [c] Estimated from the reduction potentials $E_{1/2}$, assuming the absolute energy level of ferrocene/ferrocenium to be 4.8 eV below vacuum.

gaps estimated from the absorption edge in solution. As for the LUMOs, **1** is more easily reduced than **2** and **3**, consistent with the electrochemical data.

Reorganization Energies. At room temperature, the charge transport in organic solids can be well described as a hopping mechanism because the thermal fluation and dynamic disorder effects can localize the carrier. At each step of hopping, the charge-transfer rate between two adjacent molecules can be calculated by the Marcus theory (17) in the following equation:

$$W = \frac{V^2}{h}\left(\frac{\pi}{\lambda k_B T}\right)^{1/2} \exp\left(-\frac{\lambda}{4k_B T}\right) \quad (1)$$

There are two major parameters that determine the self-exchange charge-transfer rate: the intermolecular transfer integral (V) and the reorganization energy (λ). It has been shown that the molecular reorganization energy upon accepting/donating a charge can strongly influence the charge mobility (18). The total reorganization energy λ can be expressed as the sum of two relaxation energy terms (19): (i) the difference between the energies of the neutral molecule in its equilibrium geometry and in the relaxed geometry characteristic of the ion (λ_1) and (ii) the difference between the energies of the radical ion in its equilibrium geometry and in the neutral geometry (λ_2). Table 3 displays the reorganization energies calculated at the density functional theory (DFT) level using the B3LYP functional and 6-31g(d) basis set.

The charge-transport process is considered as a cross-barrier classical mechanics motion, with a barrier height of $\lambda/4$. Here, we focus on the ET reorganization energy due to the n-type behavior of the compounds. The reorganization

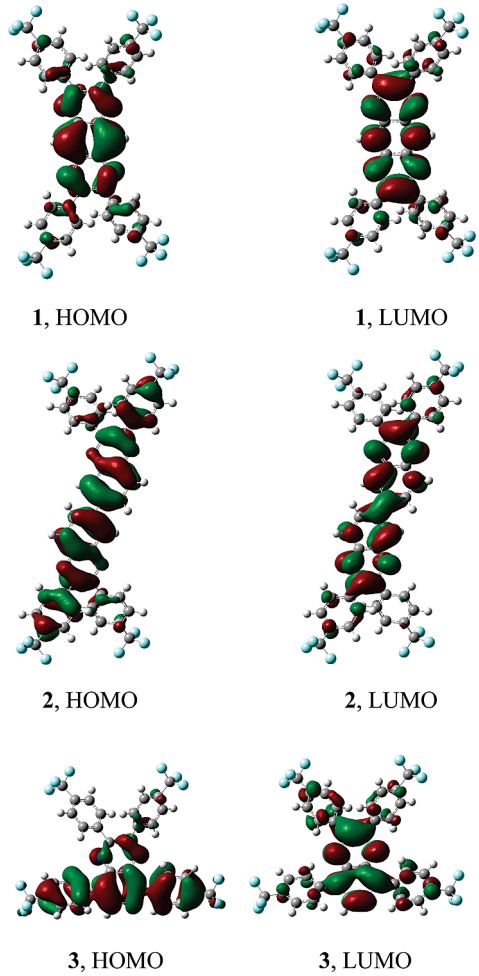

FIGURE 5. HOMOs (left) and LUMOs (right) of 1−3 obtained by DFT calculations.

Table 3. DFT-B3LYP/6-31g(d) Estimates of Hole and ET Relaxation Energies: λ_1, λ_2, and λ (in eV) from the Adiabatic Potential Surfaces of the Neutral and Charged Species

	hole			electron		
compound	$\lambda_{rel}^{(1)}$	$\lambda_{rel}^{(2)}$	λ_+	$\lambda_{rel}^{(1)}$	$\lambda_{rel}^{(2)}$	λ_-
1	0.194	0.165	0.359	0.141	0.145	0.286
2	0.146	0.140	0.285	0.147	0.139	0.285
3	0.198	0.206	0.404	0.191	0.306	0.497

energy values of **1** and **2** for ET are similar to that (0.276 eV) calculated at the same level for the well-established electron-transport material tris(8-hydroxyquinolinato)aluminum (Alq_3) (20). For **3**, the reorganization energy (0.497 eV) is larger than that of **1** and **2**, which indicates a lower ET rate and unobvious ET behavior.

Thin Film Morphology. To investigate the semiconductor film microstructure and correlate to the FET performance, X-ray diffraction (XRD) and atomic force microscopy (AFM) experiments were performed for compounds **1**−**3**. Figure 6 shows XRD patterns of **1** and **2** films deposited on octadecyltrichlorosilane (OTS)-treated SiO_2/Si substrates at room temperature. The thin film of **1** exhibits multiple families of diffraction features, suggesting good crystallinity and ordering of the thin film. **1** shows an interlayer diffraction peak at $2\theta = 4.7°$ with a d spacing of 18.7 Å, which corresponds well to the length (18.9 Å) of the molecule estimated by theory calculation, suggesting the edge-on-substrate orientation. For molecule **2**, we could not get the first-order reflection from XRD, probably because of our equipment limitation and/or weak first-order reflection. However, **2** exhibits a series of ordered reflection peaks, suggesting good crystallinity and ordering of the thin film. Surprisingly, the XRD pattern for the thin film of **3** (see Figure S1 in the Supporting Information, SI) shows only very broad peaks, suggesting no crystallinity and ordering of the thin film.

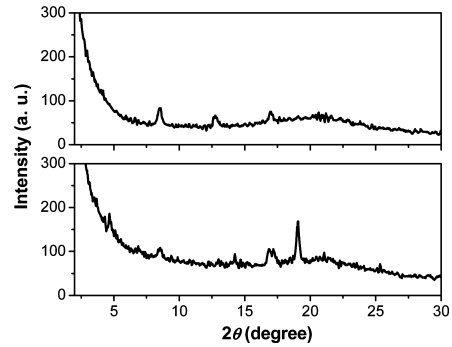

FIGURE 6. XRD patterns of evaporated thin films of 1 (bottom) and 2 (top) on OTS-treated SiO_2/Si substrates at room temperature.

We used AFM to further gain insight into the thin film morphology of compounds **1**−**3**. Figure 7 shows the AFM images of the deposited thin films of **1** and **2** at different substrate temperatures. The films of the two compounds show different morphologies. For compound **1**, a large piecelike crystalline phase with long ribbonlike islands was obtained at room temperature, while a smooth layer-by-layer structure was observed at a substrate temperature of 100 °C. Compound **2** formed clusters consisting of small crystalline grains at room temperature, while at 100 °C, the clusters are more densely packed with larger crystalline grains, which reduce the grain boundary. From the AFM image of **3** at room temperature (see Figure S2 in the SI), no crystalline domains were observed for the thin film, consistent with the XRD result.

OFET Characterization. OFET devices were fabricated in a top-contact configuration using Ag as the source and drain electrodes to study charge-transport properties of these compounds. Because of the relatively smaller EAs of these compounds than those of reported n-channel semiconductor materials, we chose the relatively low-work-function metal Ag instead of the high-work-function metal Au to facilitate electron injection, although Au electrodes are generally used to fabricate FETs. Even using Ag as the source/drain electrodes, a relatively large electron injection barrier and therefore some contact resistance still existed, evidenced by slight curvatures seen at low V_{DS} in the output plot of the FET device based on **1** (Figure 8). The mobility of devices in the saturation regime was extracted by

$$I_{DS} = (W/2L)C_i\,\mu(V_{GS} - V_{th})^2 \qquad (2)$$

where I_{DS} is the drain current, L and W are the channel length and width, respectively, C_i is the insulator capacitance per

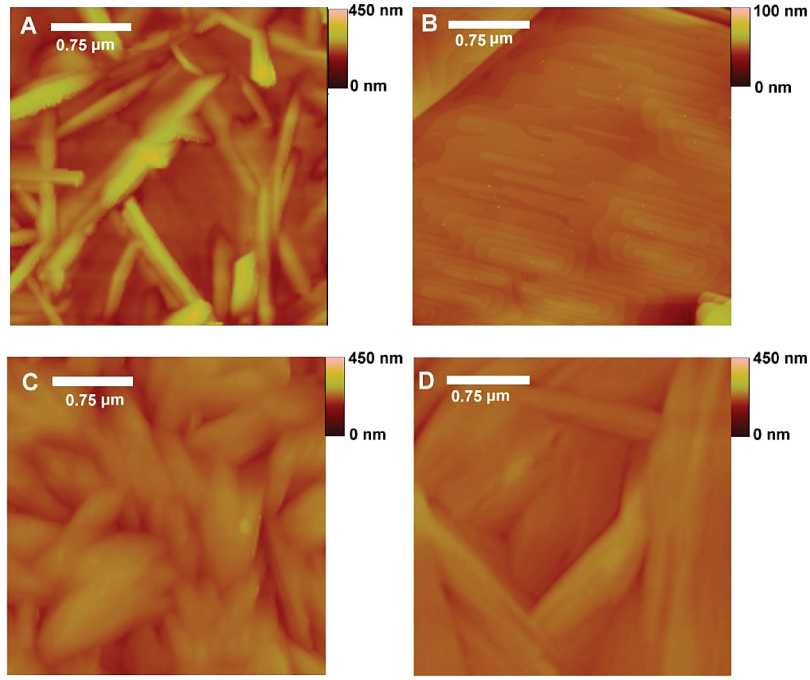

FIGURE 7. AFM images (3 μm × 3 μm) of 50-nm-thick films of 1 (top) and 2 (bottom) on OTS-treated substrates at room temperature (left) and at 100 °C (right).

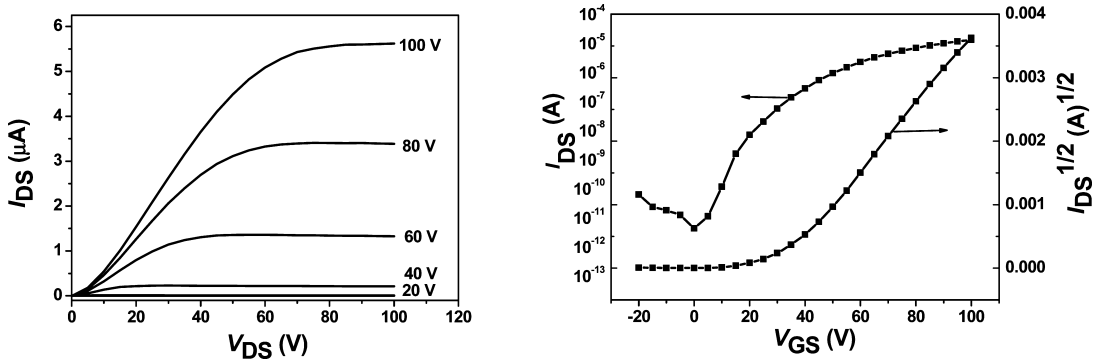

FIGURE 8. Current−voltage characteristics (I_{DS} vs V_{DS}) at several values of the gate voltage (V_{GS}) (left) and I_{DS} and $(I_{DS})^{1/2}$ vs V_{GS} plots at V_{DS} of 100 V (right) for a top contact device on a OTS/SiO_2/Si substrate with W = 3000 μm, L = 50 μm, and 50 nm thickness of 1 at 100 °C.

unit area of the gate dielectric layer, and V_{GS} and V_{th} are the gate and threshold voltages, respectively.

Compounds **1** and **2** perform as n-type semiconductors. Figure 8 shows the drain current (I_{DS}) versus drain-source voltage (V_{DS}) characteristics at several values of the gate voltage (V_{GS}) and transfer characteristics (I_{DS} vs V_{GS} plotted on a logarithmic scale and $(I_{DS})^{1/2}$ vs V_{GS}, at V_{DS} = 100 V) of the transistors based on **1** at 100 °C. The output curves show excellent saturation behavior with clear saturation currents (see Figures S3−S5 in the SI). Table 4 summarizes the effect of the substrate temperature on the FET performances of **1** and **2** under nitrogen. The electron mobilities of **1** in the saturation regime were found to be as high as 1.2×10^{-2} cm^2 V^{-1} s^{-1}; the on/off current ratio was as high as 10^6 (see Figure S3 in the SI). The device based on **2** exhibits an electron mobility of 1.5×10^{-3} cm^2 V^{-1} s^{-1} and an on/off current ratio of 10^6 (see Figure S4 in the SI). The higher mobility of **1** is attributed to its larger fused-ring core structure and higher EA. **3** did not show OFET characteristics partially because of its small core structure and deficient

Table 4. Performance of OFETs Based on 1−3 Deposited at Various Substrate Temperatures (T_{sub})

compound	T_{sub} (°C)	mobility (cm^2 V^{-1} s^{-1})	on/off ratio	threshold voltage (V)
1	25	1.2×10^{-2}	10^6	62
	100	3.1×10^{-2}	10^6	23
2	25	1.5×10^{-3}	10^6	19
	100	1.1×10^{-2}	10^6	37
3	25	no		
	100			

π-conjugated system. On the other hand, the device performance is strongly related to the film morphology. For OFETs, the charge carrier transport is influenced by the boundary density, which could trap a large amount of charge carriers. As a result, larger grains usually lead to a lower boundary density, efficient charge transport, and better device performance. In this case, the large continuous piecelike crystalline phase of **1** leads to a lower boundary density of the thin film. As a result, OFET based on **1** exhibits a higher electron mobility. For **2**, some gaps among crystalline clusters as well

as higher boundary density should be responsible for the decrease of the device performance. For **3**, the amorphous and disorder structure of the thin film is probably the main origin for no field-effect behavior.

Upon an increase in the substrate temperature, the OFET performances of **1** and **2** were improved; the mobilities of **1** and **2** are 3.1×10^{-2} and 1.1×10^{-2} $cm^2\ V^{-1}\ s^{-1}$ at 100 °C, respectively. The phenomenon is simply due to a lower boundary density as a result of larger grains at higher substrate temperatures compared with that at room temperature. The electron mobilities obtained for **1** and **2** are comparable to that reported for other pyrazine-containing derivatives (11). At room temperature, the device based on **1** exhibited a relatively high threshold voltage (V_{th}), probably due to the relatively poor film quality of **1** as evidenced by the AFM image (Figure 7). V_{th} exhibits device-to-device variations, which can be influenced by many factors including materials purity, operation atmosphere, film morphology, surface dipoles, film thickness, dielectric layer thickness, and light exposure (21). However, at 100 °C, V_{th} of **1** is lower than that of **2**, consistent with the higher EA of **1**.

We have also investigated the air stability of the devices. Unfortunately, the device performance degraded quickly in air, probably because the EAs of these compounds are too small to stabilize organic anions against water and oxygen.

To probe the effect of the trifluoromethylphenyl groups on the n-type OFETs, we synthesized 9,11,20,22-tetrazatetrabenzo[*a*,*c*,*l*,*n*]pentacene (**4**; Figure S6 in the SI), similar to **1** but without trifluoromethyl groups. Because compound **4** is insoluble in organic solvents, we could not estimate its LUMO by electrochemistry. DFT calculations suggest that the LUMO (−2.94 eV) of **4** is higher than that (−3.24 eV) of **1**, probably because of the electron-withdrawing trifluoromethyl groups in **1**. On the other hand, the trifluoromethylphenyl substituents are probably twisted from the core. Therefore, the trifluoromethylphenyl groups are considered to disturb effective intermolecular interactions. We tried to grow single crystals of compounds **1** and **2**, but unfortunately both of them were not good enough for X-ray crystallographic analysis. Thus, we cannot discuss how intermolecular interactions take place in **1** and **2** in detail. However, DFT calculations suggest that the fully fused-ring system **4** has A much lower reorganization energy for ET (0.153 eV), compared to those for **1** and **2** (ca. 0.286 eV). The device based on **4** exhibited no n-channel field-effect behavior. The distinct difference between **1** and **4** suggests that in these pyrazine systems trifluoromethylphenyl groups could be essential for the n-type OFET behavior. The trifluoromethylphenyl groups increase the EA of the pyrazine molecules and could be favorable for molecular alignment (7), although they cause A relatively large reorganization energy for ET.

CONCLUSION

To probe the thermal, electronic, optical, thin film structure, and charge-transport consequences of the cores in fused-ring pyrazine derivatives end-functionalized with trifluoromethylphenyl groups, three compounds with different pyrazine cores have been synthesized. The trifluoromethylphenyl groups increase the solubility and EA of the pyrazine molecules and could be favorable for molecular alignment, although they cause a relatively large reorganization energy for ET. Compound **1** with a larger fused-ring core exhibits lower LUMO, red-shifted absorption and emission spectra compared to **2** and **3**. Furthermore, compounds **1** and **2** with larger fused-ring cores exhibit relatively small reorganization energy and highly ordered crystalline morphology, while compound **3** with a smaller fused-ring core exhibits a large reorganization energy and disordered and amorphous morphology. The OFET devices based on compounds **1** and **2** exhibit electron mobilities as high as ca. 0.03 and 0.01 $cm^2\ V^{-1}\ s^{-1}$ under nitrogen, respectively, while **3** does not show FET characteristics. The larger pyrazine core leads to a lower LUMO level and reorganization energy, to more ordered thin film morphology with larger grain size, and finally to higher mobilities.

EXPERIMENTAL SECTION

Materials. Unless stated otherwise, starting materials were obtained from Aldrich or Acros and were used without further purification. 1,4-Dimethylpiperazine-2,3-dione (22), 2,5-dibromopyridine-3,4-diamine (23), tributyl[4-(trifluoromethyl)phenyl]stannane (24), and 9,11,20,22-tetrazatetrabenzo[*a*,*c*,*l*,*n*]-pentacene (**4**) (25) were prepared according to published procedures. THF and toluene were distilled from sodium benzophenone under nitrogen prior to use.

SYNTHESIS

4,4′-Bis(trifluoromethyl)benzil (I). To a solution of 4-bromobenzotrifluoride (110 mmol, 24.75 g) in 200 mL of dry THF was added dropwise 110 mmol (44 mL) of *n*-BuLi (2.5 M in hexanes) at −78 °C under nitrogen. After stirring at −78 °C for 1 h, to the mixture was added 1,4-dimethylpiperazine-2,3-dione (50 mmol, 7.1 g) as a powder under a nitrogen flow. The reaction mixture was gradually warmed up to room temperature and stirred at room temperature overnight. The mixture was then hydrolyzed with 300 mL of 10% HCl and extracted with CH_2Cl_2. The organic layer was dried over anhydrous $MgSO_4$, and the solvent was removed under reduced pressure. The product was purified by recrystallization from methanol to give a yellow solid (9.0 g, 52%). ^{1}H NMR (400 MHz, $CDCl_3$): δ 8.12 (d, J = 7.8 Hz, 4H), 7.81 (d, J = 8.3 Hz, 4H). ^{13}C NMR (100 MHz, $CDCl_3$): δ 191.89, 136.17 (q, $^2J_{CF}$ = 32.9 Hz), 135.18, 130.34, 126.15 (q, $^3J_{CF}$ = 3.7 Hz), 123.25 (q, $^1J_{CF}$ = 273.1 Hz). HRMS (EI). Found: *m/z* 346.0432. Calcd for $C_{16}H_8F_6O_2$: *m/z* 346.0428. Elem anal. Calcd for $C_{16}H_8F_6O_2$: C, 55.50; H, 2.33. Found: C, 55.46; H, 2.33.

5,8-Dibromo-2,3-bis(4-trifluoromethylphenyl)pyrido[3,4-*b*]pyrazine (II). A mixture of 4,4′-bis-(trifluoromethyl)benzil (10 mmol, 3.46 g) and 2,5-dibromopyridine-3,4-diamine (10 mmol, 2.89 g) in *n*-BuOH (40 mL) was refluxed under nitrogen for 16 h. After cooling to room temperature, the solvent was removed under reduced pressure, and the residue was purified by column chromatography on silica gel using 2:1 hexanes/dichloromethane as the eluent to give a pale-yellow solid (4.76 g, 83%). MS (EI): *m/z* 577 (M^+). ^{1}H NMR (400 MHz, $CDCl_3$): δ 8.83 (s, 1H),

7.91−7.74 (m, 4H), 7.73−7.57 (m, 4H). ^{13}C NMR (100 MHz, $CDCl_3$): δ 156.60, 154.33, 147.91, 146.42, 142.50, 140.06, 135.93, 132.32 (m), 130.61, 130.51, 127.69 (q, $^1J_{CF} = 273.1$ Hz), 125.78, 125.74, 120.08. Elem anal. Calcd for $C_{21}H_9Br_2F_6N_3$: C, 43.70; H, 1.57; N, 7.28. Found: C, 43.54; H, 1.62; N, 7.08.

2,3,7,8-Tetrakis[4-(trifluoromethyl)phenyl]pyrazoquinoxaline (1). A mixture of 4,4′-bis(trifluoromethyl)benzil (3 mmol, 1.04 g) and benzene-1,2,4,5-tetraamine tetrahydrochloride (1.5 mmol, 426 mg) in *n*-BuOH (30 mL) was refluxed under nitrogen for 16 h. After cooling to room temperature, the solvent was removed under reduced pressure, and the residue was purified by column chromatography on silica gel using 1:1 hexanes/dichloromethane and dichloromethane as the eluents to give a yellow solid (0.8 g, 70%). ^{1}H NMR (400 MHz, $CDCl_3$): δ 9.09 (s, 2H), 7.78 (d, $J = 8.2$ Hz, 8H), 7.71 (d, $J = 8.3$ Hz, 8H). ^{13}C NMR (100 MHz, $CDCl_3$): δ 153.73, 141.52, 140.49, 132.26 (q, $^2J_{CF} = 32.4$ Hz), 130.33, 129.58, 127.84 (q, $^1J_{CF} = 271.1$ Hz), 125.63. HRMS (EI). Found: *m/z* 758.1350. Calcd for $C_{38}H_{18}N_4F_{12}$: *m/z* 758.1340. Anal. Calcd for $C_{38}H_{18}N_4F_{12}$: C, 60.17; H, 2.39; N, 7.39. Found: C, 60.38; H, 2.76; N, 7.00.

2,2′,3,3′-Tetrakis[4-(trifluoromethyl)phenyl]-6,7′-biquinoxaline (2). A mixture of 4,4′-bis(trifluoromethyl)benzil (2.2 mmol, 0.75 g) and biphenyl-3,4,3′,4′-tetraamine (1.0 mmol, 214 mg) in *n*-BuOH (20 mL) was refluxed under nitrogen for 16 h. After cooling to room temperature, the solvent was removed under reduced pressure, and the residue was purified by column chromatography on silica gel using 1:1 hexanes/dichloromethane and dichloromethane as the eluents to give a pale-yellow solid (0.75 g, 90%). ^{1}H NMR (400 MHz, $CDCl_3$): δ 8.62 (d, $J = 1.5$ Hz, 2H), 8.37 (d, $J = 8.7$ Hz, 2H), 8.32 (dd, $J = 8.7$ Hz, 1.7 Hz, 2H), 7.72 (d, $J = 8.4$ Hz, 8H), 7.68 (d, $J = 8.4$ Hz, 8H). ^{13}C NMR (100 MHz, $CDCl_3$): δ 152.36, 151.94, 141.87, 141.67, 141.51, 141.08, 131.74 (q, $^2J_{CF} = 32.6$ Hz), 130.22, 130.17, 127.89 (q, $^1J_{CF} = 270.8$ Hz), 127.62, 125.54, 125.51. MS (MALDI): *m/z* 835 (MH^+). Elem anal. Calcd for $C_{44}H_{22}N_4F_{12}$: C, 63.32; H, 2.66; N, 6.71. Found: C, 63.58; H, 2.74; N, 6.73.

2,3,5,8-Tetrakis[4-(trifluoromethyl)phenyl]pyrido[3,4-*b*]pyrazine (3). To a solution of **II** (1 mmol, 577 mg) and tributyl[4-(trifluoromethyl)phenyl]stannane (3 mmol, 1.3 g) in dry toluene (10 mL) was added $Pd(PPh_3)_4$ (0.05 mmol, 57.8 mg) under a dinitrogen atmosphere. The mixture was stirred at 110 °C for 48 h. After cooling to room temperature, a 10 mL aqueous solution of KF (5 g) was added and stirred for 10 min. The organic layer was extracted with CH_2Cl_2 and washed subsequently with a 10% HCl aqueous solution and a saturated $NaHCO_3$ aqueous solution. The organic phase was dried over anhydrous $MgSO_4$. The product was purified by column chromatography on silica gel using 1:1 hexanes/dichloromethane and dichloromethane as the eluents and recrystallized from methanol to give a yellow solid (0.49 g, 70%). ^{1}H NMR (400 MHz, $CDCl_3$): δ 9.07 (s, 1H), 8.43 (d, $J = 8.12$ Hz, 2H), 7.99 (d, $J = 8.07$ Hz, 2H), 7.85 (d, $J = 8.17$ Hz, 4H), 7.66 (m, 8H). ^{13}C NMR (100 MHz, $CDCl_3$): δ 158.52, 154.64, 152.06, 146.79, 141.62, 140.98, 140.84, 140.48, 137.96, 133.87, 132.30, 132.06, 131.98, 131.73, 131.60, 131.31, 131.04, 130.79, 130.47, 130.35, 130.22, 125.76, 125.50, 125.40, 125.37, 125.05, 125.02, 122.80, 122.36, 122.32. HRMS (EI): *m/z* 707.1237. Calcd for $C_{35}H_{17}N_3F_{12}$: *m/z* 707.1231. Elem anal. Calcd for $C_{38}H_{18}N_4F_{12}$: C, 59.42; H, 2.42; N, 5.94. Found: C, 59.12; H, 2.78; N, 5.67.

We tried to grow single crystals of compounds **1** and **2** in chloroform, toluene, or mixed solvents (chloroform or toluene with methanol in different volume ratios) through slow evaporation of the solvents. The crystals of **1** and **2** were needles, but unfortunately both of them were not good enough for X-ray crystallographic analysis. For compound **3**, we did not try to grow single crystals.

Measurements. The ^{1}H and ^{13}C NMR spectra were measured on a Bruker Avance 400 MHz spectrometer using tetramethylsilane ($\delta = 0$ ppm) as an internal standard. Mass spectra were measured on a GCT-MS micromass (U.K.) spectrometer using the electron impact (EI) mode or on a Bruker Daltonics BIFLEX III MALDI-TOF analyzer using MALDI mode. Elemental analyses were carried out using a FLASH EA1112 elemental analyzer. Solution (dichloromethane) and thin-film (on quartz substrate) UV−vis absorption spectra were recorded on a Jasco V-570 spectrophotometer. Solution (dichloromethane) and thin-film (on quartz substrate) emission spectra were collected on a Hitachi F-4500 spectrofluorophotometer. Electrochemical measurements were carried out under nitrogen on a deoxygenated solution of tetra-*n*-butylammonium hexafluorophosphate (0.1 M) in dichloromethane using a computer-controlled Zahner IM6e electrochemical workstation, a glassy-carbon working electrode, a Pt-wire auxiliary electrode, and a Ag wire anodized with AgCl as a pseudoreference electrode. Potentials were referenced to the ferrocenium/ferrocene ($FeCp_2^{+/0}$) couple by using ferrocene as an internal standard. TGA measurements were performed on a Shimadzu thermogravimetric analyzer (model DTG-60) under a nitrogen flow at a heating rate of 10 °C min^{-1}. The film morphology was analyzed in air using a Nanoscope III atomic force microscope (Digital Instruments) operated in tapping mode. XRD of thin films was performed in the reflection mode at 40 kV and 200 mA with Cu Kα radiation using a 2 kW Rigaku D/max-2500 X-ray diffractometer.

Fabrication and Characterization of Field-Effect Transistors. OFET devices were fabricated with a top-contact configuration. A heavily doped n-type Si wafer with a 500 nm-thick layer of thermally grown SiO_2 and a capacitance of 7.5 nF cm^{-2} was used as the gate. Octadecyltrichlorosilane (OTS) was used as a self-assembled surface modifier for SiO_2. Thin films of **1**−**3** (50 nm) were formed on the OTS-modified substrates by high-vacuum evaporation. After that, the Ag source and drain contacts (50 nm) were deposited onto the organic layer through a shadow mask under high vacuum. The channel length (*L*) and width (*W*) were 50 μm and 3 mm, respectively. The samples were transferred in a vacuum-tight vessel without being exposed

to atmospheric conditions into a nitrogen glovebox (O_2, H_2O < 1 ppm) for electrical testing. All of the measurements of electric properties were carried out at room temperature using a Keithley 4200 SCS semiconductor parameter analyzer. To investigate the effect of the substrate temperatures on the device performance, the semiconductors **1**−**3** were vacuum-deposited onto the substrate with controlled temperatures of 25 and 100 °C.

Computation. DFT calculations were carried out using *Gaussian 03* (26) at the B3LYP/6-31g(d) level (27).

Acknowledgment. We thank the Ministry of Science and Technology of China (Grant 2006CB932100), the National Natural Science Foundation of China (Grants 50873107, 20721061, and 60736004), and the Chinese Academy of Sciences for financial support.

Supporting Information Available: XRD pattern and AFM image of a thin film of **3** on an OTS-treated SiO_2/Si substrate, output and transfer characteristics of OFETs based on **1** and **2**, and the chemical structure of **4**. This material is available free of charge via the Internet at http://pubs.acs.org.

REFERENCES AND NOTES

(1) (a) See reviews: Sun, Y.; Liu, Y.; Zhu, D. *J. Mater. Chem.* **2005**, *15*, 53. (b) Di, C.; Yu, G.; Liu, Y.; Zhu, D. *J. Phys. Chem. B* **2007**, *111*, 14083. (c) Murphy, A. R.; Frechet, J. M. J. *Chem. Rev.* **2007**, *107*, 1066. (d) Zaumseil, J.; Sirringhaus, H. *Chem. Rev.* **2007**, *107*, 1296.

(2) Tsumura, A.; Koezuka, H.; Ando, I. *Appl. Phys. Lett.* **1986**, *49*, 1210.

(3) (a) Muccini, M. *Nat. Mater.* **2006**, *5*, 605. (b) Allard, S.; Forster, M.; Souharce, B.; Thiem, H.; Scherf, U. *Angew. Chem., Int. Ed.* **2008**, *47*, 4070.

(4) (a) Christopher, R. N.; Frisblie, C. D.; Demetrio, A.; da Filho, S.; Brédas, J.-L.; Ewbank, P. C.; Mann, K. R. *Chem. Mater.* **2004**, *16*, 4436. (b) Babel, A.; Jenekhe, S. A. *J. Am. Chem. Soc.* **2003**, *125*, 13656. (c) Zhan, X.; Tan, Z.; Domercq, B.; An, Z.; Zhang, X.; Barlow, S.; Li, Y.; Zhu, D.; Kippelen, B.; Marder, S. R. *J. Am. Chem. Soc.* **2007**, *129*, 7246.

(5) (a) Tang, M. L.; Reichardt, A. D.; Miyaki, N.; Stoltenberg, R. M.; Bao, Z. *J. Am. Chem. Soc.* **2008**, *130*, 6064. (b) Facchetti, A.; Mushrush, M.; Yoon, M.-H.; Hutchison, G. R.; Ratner, M. A.; Marks, T. J. *J. Am. Chem. Soc.* **2004**, *126*, 13859. (c) Letizia, J. A.; Facchetti, A.; Stern, C. L.; Ratner, M. A.; Marks, T. J. *J. Am. Chem. Soc.* **2005**, *127*, 13476. (d) Sakamoto, Y.; Suzuki, T.; Kobayashi, K.; Gao, Y.; Fukai, Y.; Inoue, Y.; Sato, F.; Tokito, S. *J. Am. Chem. Soc.* **2004**, *126*, 8138. (e) Handa, S.; Miyazaki, E.; Takimiya, K.; Kunugi, Y. *J. Am. Chem. Soc.* **2007**, *129*, 11684.

(6) Cornil, J.; Beljonne, D.; Calbert, J.-P.; Brédas, J.-L. *Adv. Mater.* **2001**, *13*, 1053.

(7) (a) Ando, S.; Murakami, R.; Nishida, J.; Tada, H.; Inoue, Y.; Tokito, S.; Yamashita, Y. *J. Am. Chem. Soc.* **2005**, *127*, 14996. (b) Ando, S.; Nishida, J.; Tada, H.; Inoue, Y.; Tokito, S.; Yamashita, Y. *J. Am. Chem. Soc.* **2005**, *127*, 5336. (c) Mamada, M.; Nishida, J.; Kumaki, D.; Tokito, S.; Yamashita, Y. *Chem. Mater.* **2007**, *19*, 5404. (d) Kono, T.; Kumaki, D.; Nishida, J.; Sakanoue, T.; Kakita, M.; Tada, H.; Tokito, S.; Yamashita, Y. *Chem. Mater.* **2007**, *19*, 1218. (e) Akhtaruzzaman, M.; Kamata, N.; Nishida, J.; Ando, S.; Tada, H.; Tomura, M.; Yamashita, Y. *Chem. Commun.* **2005**, 3183. (f) Akhtaruzzaman, M.; Tomura, M.; Nishida, J.; Yamashita, Y. *J. Org. Chem.* **2004**, *69*, 2953. (g) Kojima, T.; Nishida, J.; Tokito, S.; Tada, H.; Yamashita, Y. *Chem. Commun.* **2007**, 1430.

(8) (a) Tonzola, C. J.; Alam, M. M.; Kaminsky, W.; Jenekhe, S. A. *J. Am. Chem. Soc.* **2003**, *125*, 13548. (b) Gao, B.; Wang, M.; Cheng, Y.; Wang, L.; Jing, X.; Wang, F. *J. Am. Chem. Soc.* **2008**, *130*, 8297.

(9) Winkler, M.; Houk, K. N. *J. Am. Chem. Soc.* **2007**, *129*, 1805.

(10) (a) Kestemon, G.; Halleux, V.; Lehmann, M.; Ivaanov, D. A.; Watson, M.; Geerts, Y. H. *Chem. Commun.* **2001**, 2074. (b) Hu, J.; Zhang, D.; Jin, S.; Cheng, Z. D.; Harris, F. W. *Chem. Mater.* **2004**, *16*, 4912. (c) Kaafarani, B. R.; Kondo, T.; Yu, J.; Zhang, Q.; Dattilo, D.; Risko, C.; Jones, S. C.; Barlow, S.; Domercq, B.; Amy, F.; Kahn, A.; Brédas, J.-L.; Kippelen, B.; Marder, S. R. *J. Am. Chem. Soc.* **2005**, *127*, 16358. (d) Ishi-i, T.; Yaguma, K.; Kuwahara, R.; Taguri, Y.; Mataka, S. *Org. Lett.* **2006**, *8*, 585. (e) Zhu, Y.; Yen, C.-T.; Jenekhe, S. A.; Chen, W. C. *Macromol. Rapid Commun.* **2004**, *25*, 1829.

(11) (a) Nishida, J.-I.; Naraso, S. M.; Fujiwara, E.; Tada, H.; Tomura, M.; Yamashita, Y. *Org. Lett.* **2004**, *6*, 2007. (b) Nakagawa, T.; Kumaki, D.; Nishida, J.; Tokito, S.; Yamashita, Y. *Chem. Mater.* **2008**, *20*, 2615. (c) Naraso; Nishida, J.; Kumaki, D.; Tokito, S.; Yamashita, Y. *J. Am. Chem. Soc.* **2006**, *128*, 9598.

(12) Xiao, K.; Liu, Y. Q.; Qi, T.; Zhang, W.; Wang, F.; Gao, J. H.; Qiu, W. F.; Ma, Y. Q.; Cui, G. L.; Chen, S. Y.; Zhan, X. W.; Yu, G.; Qin, J. G.; Hu, W. P.; Zhu, D. B. *J. Am. Chem. Soc.* **2005**, *127*, 13281.

(13) (a) Anthony, J. E. *Chem. Rev.* **2006**, *106*, 5028. (b) Anthony, J. E. *Angew. Chem., Int. Ed.* **2008**, *47*, 452.

(14) Yakeshi, T.; Goto, T.; Fujita, K.; Tsutsui, T. *Appl. Phys. Lett.* **2004**, *85*, 2098.

(15) (a) Jang, B. B.; Lee, S. H.; Kafafi, Z. H. *Chem. Mater.* **2006**, *18*, 449. (b) Brusso, J. L.; Hirst, O. D.; Dadvand, A.; Ganesan, S.; Cicoira, F.; Robertson, C. M.; Oakley, R. T.; Rosei, F.; Perepichka, D. F. *Chem. Mater.* **2008**, *20*, 2484.

(16) Takimiya, K.; Kunugi, Y.; Toyoshima, Y.; Otsubo, T. *J. Am. Chem. Soc.* **2005**, *127*, 3605.

(17) (a) Marcus, R. A. *Annu. Rev. Phys. Chem.* **1964**, *15*, 155. (b) Marcus, R. A. *Rev. Mod. Phys.* **1993**, *65*, 599.

(18) Yang, X. D.; Wang, L. J.; Wang, C. L.; Long, W.; Shuai, Z. G. *Chem. Mater.* **2008**, *20*, 3205.

(19) Berlin, Y. A.; Hutchinson, G. R.; Rempala, P.; Ratner, M. A.; Michl, J. *J. Phys. Chem. A* **2003**, *107*, 3970.

(20) Lin, B. C.; Cheng, C. P.; You, Z.-Q.; Hsu, C.-P. *J. Am. Chem. Soc.* **2005**, *127*, 66.

(21) Jones, B. A.; Facchetti, A.; Wasielewski, M. R.; Marks, T. J. *J. Am. Chem. Soc.* **2007**, *129*, 15259.

(22) (a) Mueller-Westerhoff, U. T.; Zhou, M. *Tetrahedron Lett.* **1993**, *34*, 571. (b) Mueller-Westerhoff, U. T.; Zhou, M. *J. Org. Chem.* **1994**, *59*, 4988.

(23) Lee, B. L.; Yamamoto, T. *Macromolecules* **1999**, *32*, 1375.

(24) Kozyrod, R. P.; Morgan, J.; Pinhey, J. T. *Aust. J. Chem.* **1985**, *38*, 1147.

(25) Reimschuessel, H. K.; Boardman, F. U.S. Patent 3,403,154, 1968; *Chem. Abstr.* **1969**, *70*, 20988b.

(26) Frisch, M. J.; et al. *Gaussian 03*, revision A.1; Gaussian, Inc.: Pittsburgh, PA, 2003.

(27) Brédas, J. L.; Beljonne, D.; Cornil, J.; Calbert, J. P.; Shuai, Z.; Silbey, R. *Synth. Met.* **2001**, *125*, 107.

AM900093P